Genetic Effects on Structural and Functional Properties of Sensorimotor-Association Axis of Cortical Organization are Selectively Distinct

Giacomo Bignardi[1,2*], Michel G. Nivard[3], H. Lina Schaare[4,5], Boris C. Bernhardt[6], Richard A.I. Bethlehem[7,8], Simon E. Fisher[1,9,†], & Sofie L. Valk[4,5,10,† *]

[1] Language and Genetics Department, Max Planck Institute for Psycholinguistics, Nijmegen, The Netherlands;
[2] Max Planck School of Cognition, Leipzig, Germany;
[3] Department of Biological Psychology, Faculty of Behaviour and Movement Sciences, VU University, Amsterdam, The Netherlands;
[4] Max Planck Institute for Human Cognitive and Brain Sciences, Leipzig, Germany;
[5] Research Center Jülich, Institute for Neuroscience and Medicine (INM-7), Germany;
[6] McGill University, Montreal, Canada;
[7] Autism Research Centre, Department of Psychiatry, University of Cambridge, Cambridge, United Kingdom;
[8] Department of Psychology, University of Cambridge, Cambridge, United Kingdom;
[9] Donders Institute for Brain, Cognition and Behaviour, Radboud University, Nijmegen 6500 HB, The Netherlands;
[10] Heinrich-Heine-Universitaet Duesseldorf, Germany

* Giacomo Bignardi
* Sofie L Valk.
† These authors share last authorship.
Email: giacomo.bignardi@mpi.nl; valk@cbs.mpg.de

Author Contributions: S.L.V. and G.B. conceptualised the work; S.L.V. & S.E.F. supervised the research; G.B. performed primary analyses; S.L.V., S.E.F, M.G.N, B.C.B., and R.A.I. gave input on analysis and Figures; S.L.V. performed functional connectomics, microstructural and geodesic distance analysis; H.L.S. provided input in diffusion map embedding analysis; G.B. computed Figures; G.B, & S.L.V. drafted the manuscript; S.L.V., S.E.F, M.G.N, B.C.B., H.L.S., and R.A.I. contributed to revising the manuscript.

Competing Interest Statement: The authors declare no competing interest.

Keywords: Neuroscience, Sensorimotor-Association axis, Behaviour Genetics, Structural Equation Modeling, Measurement Error.

This file includes:

Main Text
Figures 1 to 5

Abstract

The topological differentiation of sensorimotor and association cortical regions along a sensorimotor-association (S-A) axis has undergone profound evolutionary change along the mammalian lineage. In humans, patterns of gene expression, microstructure, and functional connectivity have been shown to vary systematically along such S-A axis. Despite robust spatial relationships between these different neurobiological traits, whether common genetic pressures shape the S-A axis across traits remains poorly understood. In this study, we exploit observed pervasive inter-individual variation in the S-A axis to capture its genetic architecture and to study shared common genetic sources of structure-function relationships. To do so, we applied a structural equation modeling framework, which reduced the issue of measurement error heterogeneity across the cortex and its impact on structure-function relationship estimates. We then used genetic relatedness across pairs of twins and removed intra-individual differences to focus on the reliable inter-individual differences along the S-A functional axis. Notwithstanding robust spatial relationships and highly heritable inter-individual differences in S-A axis microstructure and functional organisation, and contrary to group-level findings, our results indicate distinct genetic effects across the different S-A axis properties. Together, our observations challenge the notion of a common genetic cause for the association between S-A axis structural and functional properties. Our approach highlights the diversity of genetic origins of brain features that co-vary along the S-A axis, which is key to interrogating inter-individual variability in brain organisation and its consequences on cognition.

Introduction

The human brain supports perception and action but also abstract cognition (1, 2). This diversity of functions is thought to be reflected by the gradual dissociation between unimodal sensory and transmodal association cortical areas along a sensorimotor-association (S-A) axis (3). The S-A axis spans a vast array of neuroanatomical properties, including microstructural variation (myelination and cytoarchitecture) and inter-areal connectivity distance (1, 3–6). Here, sensory areas show increased microstructural differentiation, myelination, and, predominantly, short-range connections. In contrast, association areas show less differentiated microstructural profiles, reduced myelination, and a combination of short- and long-range connectivity profiles (5, 7, 8). The S-A axis underwent profound evolutionary changes (3), with an expansion of cortical association areas paralleled by a marked laminarisation of sensory areas in human primates (9, 10). Such structural re-organisation and evolutionary changes along the S-A axis (1, 6, 11, 12) may have provided the scaffold for functional differentiation (13, 14), allowing in turn for human-specific cognitive and behavioural flexibility (1, 13).

In recent years, several discoveries have enhanced our understanding of the link between structural and functional features of the S-A axis. These findings have highlighted spatial associations between microarchitectonic differentiation (15) and cortical geometry (16) with intrinsic functional organisation (13, 17). For example, T1w/T2w maps derived from non-invasive Magnetic Resonance Imaging (MRI)—indexing cortical microstructural differences—have been shown to relate strongly to gene transcriptional profiles and functional dissociation along the S-A axis. This suggests that a canonical genetic architecture may shape S-A axis structural organisation, in turn allowing for the differentiation of cortical function (6). However, despite well-documented strong associations at the group-level (3, 4, 6, 18), it is still unclear whether common genetic pressure across different structural and functional features influences S-A axis variability between individuals. Therefore, here we asked whether common genetic effects are expected to shape structural and functional properties of the S-A axis similarly or whether, alternatively, genetic sources on S-A properties are distinct.

To answer our question, we first studied whether the S-A axis's structural and functional properties correlate. To do so, we shifted the focus of the analysis from the group to the individual level. First, we asked: do individual differences in structural properties of the S-A axis relate to differences in functional properties? In other words, we studied whether previously widely reported group averages can inform S-A axis associations at the individual level. Answering this question is a crucial step towards understanding the genetic architecture of the S-A axis, as individual differences can be further used as a window into the genetic basis of a trait (19). Specifically, we tested whether individual regional cortical microstructure (6) and structural cortico-cortical network proximity (20), captured by the geodesic distance of inter-connected regions across the cortical mantle (1, 20), relate to the well-known functional dissociations between sensory and transmodal association areas (1, 3). To account for the known issue of measurement error heterogeneity across the cortex (21) and its impact on association estimates (22), we applied and adapted measurement error models in the form of structural equation models (23, 24). This allowed us to tease apart unreliable intra-individual from reliable inter-individual variation in the

121 functional organisation of the S-A axis. We then moved to answer our main question: Are genetic effects
122 on the S-A axis shared across structural and functional properties? Here, we analysed a genetic
123 informative sample and quantified the extent of overlap across genetic effects on structural and
124 functional properties of the S-A axis. Specifically, we used a twin-informed design to tease genetic
125 overlaps between the S-A axis's structural and functional properties. Last, we evaluated the robustness
126 of our results, both across subsamples, between regional and global cortical metrics, and between and
127 within individuals' S-A axis properties.
128
129 In summary, our study describes the specificity of genetic effects underlying the brain's different
130 structural and functional properties. This can inform further studies on the genetic origins of fundamental
131 principles of brain organisation and pave the way for research on the relationship between individual
132 variability in brain organisation principles and cognitive-behavioural differences.
133
134 **Results**
135 To quantify structural and functional S-A axis properties, we combined microstructural and resting-state
136 functional MRI (rsfMRI) data from the Human Connectome Project (HCP (25); *N*=992 adults; 529
137 women, mean age 28 y; 22-37 y). We computed two structural metrics and one functional metric
138 indexing the S-A axis:
139
140 • Regional microstructure: we quantified regional microstructure indexing the differentiation
141 between sensorimotor and association areas using the individuals' mean intensity of regional
142 T1w/T2w ($T1w/T2w_{mi}$) in 400 parcels (6, 26)
143 • Geodesic distance: we quantified regional cortico-cortical network proximity (20) by computing
144 the Geodesic Distance (GD) between every cortical region and its corresponding functional
145 network, averaging within each region to get parcel-wise estimates (27)
146 • Functional gradient loadings: we quantified individuals' functional S-A axis by obtaining the first
147 component of the individual functional connectomes (FC_{G1}) using diffusion map embedding (1)
148
149 We started our analysis by testing whether associations between group-level averaged maps of
150 structural S-A axis properties correlated with the functional S-A axis (Fig. 1A-C). By using a subsample
151 of *n* = 482 adults (229 women, mean age 28 y; 22-37 y; a subsample obtained by excluding respective
152 all twins included in the full HCP sample), we were able to replicate group-level findings between
153 averaged $T1w/T2w_{mi}$ and FC_{G1}, extending the results to GD and FC_{G1} (Fig. 1D-E).
154
155 [Fig. 1 here]
156
157 **Pervasive inter-individual differences in the S-A axis of cortical organisation.** Having estimated
158 the extent of overlap between structural and functional S-A axis properties at the group-level, we shifted
159 the focus to the individual level. Since group-level S-A axis can mask substantial individual variability
160 (Fig. 2A), we asked: does individual variability in structural S-A axis properties relate to variability in S-

A functional properties, as for group-level analysis (Fig. 2B)? By shifting analysis from group-level summary statistics to individual variability, we harnessed the fundamental distinction between intra- and inter-individual differences (28). The first is known to index unreliable and fluctuating variability within individuals over time, while the second indexes the reliable and stable part of the overall variability between individuals (Fig. 2C) (28). This distinction is crucial, as intra-individual variability can downward bias effect sizes, reduce statistical power (28), additionally downward biasing genetic estimates (29), all of the above heterogeneously across the whole cortex (21), and can, therefore, increase reproducibility issues (see (22) for details). We were able to make such a distinction by exploiting one of the strengths of the HCP design, which emphasises multiple resting-state fMRI sessions (across two days of scanning sessions, ~30 min each). This feature of the HCP design allowed us to discard unreliable intra-individual fluctuations in rsfMRI data from reliable inter-individual differences in the functional gradient. Precisely, we partition the inter-individual variance ($\sigma_{inter}^2 FC_{G1i}$) from the overall observed variance in the functional gradient ($\sigma^2 FC_{G1i}$ for any parcel *i*) by applying a measurement error model ((23, 24) Fig. 2D, see Methods).

Estimates obtained from the measurement error model indicate that 33% of the total variability in the functional gradient was, on average, accounted for by intra-individual variance (Fig. 2E) even when using individual functional gradients extracted from functional connectomes averaged across two days of rsfMRI sessions (totalling ~60 min of scanning session). In other words, estimates for the association between the functional gradient and other S-A axis properties (or any other variable) would be, on average, biased downward by a factor of bias(*r*-observed, *r*-true) = 0.82 (a lower bound calculated assuming perfect reliability for the other S-A axis property (22)). Second, we observed systematic differences in estimates obtained from the measurement models across functional cortical networks, $F(6, 393) = 33.21$, $p < .001$; $\eta^2 = 0.34$, 95% CI [0.27, 1.00]), with estimates for parcel-wise inter-individual variances ranging from $\sigma_{inter\text{-}114}^2 = .39$ to $\sigma_{inter\text{-}294}^2 = .89$ (Figure 2D, SI Appendix, Fig. S1). In other words, bias is heterogeneous and expected to influence estimates across the cortex systematically.

[Fig. 2 here]

Individual differences in regional cortico-cortical network proximity, rather than microstructure, relate to the functional gradient of the S-A axis of cortical organisation. To simultaneously de-attenuate the heterogenous downward biases and handle structural and functional S-A metrics, we used a Structural Equation Modeling (SEM) approach. Precisely, we specified a model in which the inter-individual differences in the functional gradient estimated via the measurement error model were directly tested for associations with microstructural profiles and geodesic distances parcel-wise data (Fig. 3A). Here, we note that we avoided making assumptions about the causal structure generating the possible correlations between structural and functional metrics. We simply limited ourselves to estimating the association between regional properties of the S-A axis. On the one end, conversely to group-level topographies, we found less than 2% of the 400 parcels to display a significant association between individuals' microstructural profiles and functional gradient loadings (Fig. 3B). These significant

associations were all negative, weak (-.20 > r > -.27), and spread across both hemispheres and the dorsal, ventral, and default-mode functional networks. Conversely, we found large overlaps between individual geodesic distances and functional gradient loadings (Fig. 3C), with 57% of the 400 parcels showing significant associations after Bonferroni correction. The directionality of the estimates for the association between individual regional geodesic distances and functional gradient loadings highlighted systematic differences across functional networks. Significant positive associations were preferentially clustered within the visual and the default mode (one sample t-test, two-sided, $t(21) = 5.82$, $p < .001$, average $r = .51$, and $t(53) = 4.04$, $p = .001$, average $r = .25$), while negative associations where preferentially clustered within the somatomotor and ventral attention networks (one sample t-test, two-sided, $t(59) = -13.32$, $p < .001$, average $r = -.48$, and $t(27) = -8.14$, $p < .001$, average $r = -.40$, respectively, all test corrected for Bonferroni). Estimates obtained from standard correlation analysis further confirmed that the SEM approach successfully de-attenuated measurement error bias (SI Appendix, Fig. S2).

[Fig. 3 here]

Genetic effects on regional S-A axis variability are substantial yet mostly distinct. After having related inter-individual differences in structural and functional S-A axis properties, we asked whether genetic effects were mostly common or distinct across S-A axis properties. Here, we further exploited the HCP's family structure to partition the relationship between structural and functional properties of the S-A axis in common and distinct genetic sources. Precisely, by applying a multivariate twin design, we were able to partition genetic ($\sigma^2_{A;}$ A: additive) and unsystematic environmental ($\sigma^2_{E;}$ E: Unique-Environmental) sources of variability in microstructure, geodesic distances, and functional gradients loadings. (Here, we note that since intra-individual variability is partitioned in the E component of the model (30), this strategy made it also possible to discard further intra-individual sources of variance in structural metrics, even in the absence of repeated measures (29)). To do so, we focused our analysis on the twin HCP subsample, which includes both monozygotic (MZ) and dizygotic (DZ) twins (n = 328, 195 MZ and 133 DZ individual twins, 124 and 88 women, respectively; mean age 29 y, range=22-35 y; see Methods for details on inclusion criteria).

To partition sample variability ($\sigma^2_{p;}$ p: S-A axis phenotypic property) within S-A modalities in σ^2_A and σ^2_E sources and further unpack genetic and environmental structure-function associations, we specified a multigroup multivariate model with only A and E components (Fig. 4A). Microstructural profiles, geodesic distances, and functional gradients loadings all displayed substantial heritability (h^2_{twin}), with mean h^2_{twin} =.43, sd =.11, mean h^2_{twin} =.34, sd =.11, and mean h^2_{twin} =.57, sd =.14, respectively. Consistent with previous work (24), a comparison of univariate models fitted to functional gradient loadings not accounting for measurement error confirmed that the inclusion of the measurement error model substantially boosted h^2_{twin} estimates of 54% relative to h^2_{twin} not accounting for intra-individual variance (univariate h^2_{twin} = .37, sd =.11 when not including a measurement error model, see SI Appendix, Fig. S3). However, notwithstanding such relatively high h^2_{twin} for both microstructural profiles

and functional gradient loadings, we found no significant additive genetic correlation between the two (all $p > .05$, Bonferroni corrected; Fig. 4B). This suggested little room for possible common genetic causes between microstructural intensity and functional gradient loadings S-A axis properties. Conversely, 14% of the parcels displayed significant additive genetic correlations between geodesic distances and functional gradient loadings (7% negative and 6% positive in directionality, respectively $p < .05$, Bonferroni corrected, Fig. 4C). The average magnitude of the genetic correlation (r_A) was r_A = -0.67, *sd* = .16, and r_A = .64, *sd* = .16, for the negative and positive association, respectively. Furthermore, we found that for 30% of the parcels, complementary environmental effects mostly correlated between geodesic distances and functional gradient loadings.

[Fig. 4 here]

Associations between structural and functional properties of the S-A axis are robust across samples. To test for the robustness of the results discussed so far, we estimated the overlap of the significant regional genetic or environmental association in the genetically informative subsample with the significant regional associations obtained from the first subsample. Of the 104 parcels that displayed either or both significant genetic and environmental correlations between geodesic distances and functional gradient loadings in the genetically informative sample, 99 also displayed a significant correlation in the first subsample. In other words, we found a 95% overlap between subsamples. These results show that regional results were robust across two subsamples drawn from the HCP.

Genetic and environmental associations extend beyond regional S-A axis variability. As a final analysis, we asked whether associations between geodesic distances and functional gradients were generalisable beyond regional differences. First, we quantified global S-A axis properties variability as the overall Median Absolute Deviation (MAD) across all parcels within individuals. Within an individual, higher MAD scores indicate a larger dispersion in S-A axis values across the cortex. Once more, we found no significant genetic or environmental associations between microstructural profile intensity and functional gradients. Yet, we found a substantial negative genetic correlation between the geodesic distances and functional gradient between individuals' S-A axis MAD scores (r_A = -.78, 95% CI [-1.19, -.34], CFI = .93, RMSEA = 0.04; Fig. 5A). Additionally, to get a complementary estimate of global S-A axis variability, we quantified microstructural profile intensity, geodesic distance, and functional gradient ρ similarity indices. These indices assessed how similar S-A axis properties in one individual are compared to the average. Consistent with regional and global variances differences, ρ similarity indices in geodesic distance, rather than microstructure, showed strong and positive genetic correlations with global differences in the functional gradient (r_A = .61, 95% CI [.43, .79], CFI = .95, RMSEA = 0.04; Fig. 5B). Findings were robust to ICV as a possible common cause of S-A axis structure-function covariance (SI Appendix, Fig. S4)

[Fig. 5 here]

Discussion

Notwithstanding the relatively high heritability of the S-A axis properties as shown in this study, theoretical models of S-A axis development and evolution (3), and group-level relationships between patterns of gene expression, cortical microstructure, and functional differentiation of sensorimotor to transmodal-association areas (6), we found little evidence for shared genetic effects between microstructural and functional S-A axis similarities. Precisely, we found little evidence of phenotypic and an absence of evidence for genetic or environmental associations between cortical microstructure (as measured by T1w/T2w) and S-A function (as measured by the principal gradient of functional connectivity) of the cortex. These results, which accounted for measurement error and held across regional and global cortical metrics and between and within individuals, do not support the hypothesis of substantial common genetic pressure on S-A axis microstructural and functional similarities.

At the same time, our results showed substantial genetic and environmental associations between individual-level differences in regional and global cortico-cortical network proximity (as measured by the geodesic distance of inter-connected regions across the cortical mantle) and function. These latter results align with theories emphasising geometric constraints of brain function yet do not fully align with previous and current group-level estimates. While group-level associations indicate a positive relationship between cortico-cortical network proximity, our results indicate a mixture of positive and negative relationships at the individual level of analysis (the former preferentially clustered within the visual and default mode network, the latter with the somatomotor and the ventral attention network). Moreover, we found negative, not positive, genetic correlations when shifting from local to global association, as we did when analysing overall within-individual S-A axis dispersion. This suggests that genetic differences between people that tend to co-occur with decreased variation in geodesic distances across the cortex also tend to co-occur with more dispersed functional gradients. These results, in line with the results obtained by analysing microstructural differences between individuals, collectively reveal that group-level estimates, such as the ones previously reported in the literature, might mask pervasive inter-individual differences. These inter-individual differences, in turn, might display different patterns of associations to the one depicted at the group level.

Based on group-level associations, previous work suggested that cortical maturation of diverse neurobiological properties proceeds along a conformed evolutionarily and developmentally rooted S-A axis of cortical organisation (3, 4). However, our results indicate that genetic variants within a population are selectively associated with some properties (e.g., function and cortico-cortical network proximity) but not others (e.g., microstructure). This selective distinctness of the genetic correlates of structural and functional properties of the S-A axis might indicate that common genetic pressures influencing the development of the S-A axis across cortical properties reached fixation in the population and, therefore, are not detectable using analysis at the level of the individuals. Another possible explanation for our results may lie in the physiological and cognitive implication of the resting state signal and downstream effects on its functional gradient. It is possible that, although generally resting state networks are topologically organised along the S-A axes, their individual fluctuations reflect physiological variability

not captured by its microstructural scaffold (31). Indeed, various works have reported network integration and segregation to align with neural gain, which could be explained by alterations in neuromodulatory systems (32, 33).

While these findings may provide little information on the shared genetic pressure that gives rise to the development of the S-A axis at the group level, they could be particularly relevant for studies on the origin of differences between individuals, such as in various neuropsychiatric disorders or work on brain-behaviour associations in general. For example, recent studies noted a compression of the S-A functional axis in individuals with autism (27), schizophrenia (34), and depression (35), highlighting an association between atypical cortical functional segregation and psychiatric conditions. Complementing the latter studies with informative genetic models of structural and functional S-A axis variability would allow us to see whether and which genetic effects on S-A variability might partially explain psychiatric conditions, facilitating mechanistic insights in notoriously complex phenotypes. We also note that these models can be easily applied to many neurobiological properties (e.g., resting-state fMRI, see (24)) to enhance current brain-behaviour mapping efforts (36). To facilitate such endeavours, we have made all the code available and provided all SEM functions in R and lavaan syntax to apply multivariate twin and measurement error modelling.

The measurement error modeling approach can successfully tease apart unstable intra-individual differences from stable inter-individual differences, and this effect can have a substantial downstream impact on estimates. For example, applying the measurement error modeling approach, in line with previous results, resulted in a nearly 1.5-fold increase in heritability. We foresee that this approach could have further direct application in the undergoing research on the origins of psychiatric disorders and brain-behaviour studies and in the analysis of the genomic architecture of principles of brain organisation, for example, by mitigating the impact of measurement error heterogeneity on estimates. Indeed, when individual variability in the S-A axis is the predictor of interest, such as in brain-behaviour studies, applying any measurement error model is expected to deattenuate downwardly biased estimates (22, 28, 37, 38). Moreover, genome-wide association studies could easily implement genome-wide or genomic structural equation modeling (39, 40) extension of our approach to discard unstable and unreliable variance, overcoming attenuation biases in single nucleotide polymorphism to phenotype association (e.g., similarly to what has been done for polygenic indices based analyses (38)). However, even when these tools are applied to overcome attenuation biases in brain-behaviour association studies, associations should still be expected to be small (36). Therefore, caution should still be applied when designing a study.

It is worth noting that our study comes with the limitation of an absence of repeated measures for structural metrics. Although applying a measurement error model allowed us to disentangle intra- to inter-individual variability in functional gradient loadings, we could not account for the differences in structural properties within individuals. This limitation may have attenuated the estimated relationship between structure and function. However, the nature of the metrics and the twin design employed to

elucidate differences between individuals should mitigate the impact of such a lack of repeated structural metrics (29). By applying the classical twin design, we were able to further partition unstable measurement error in the environmental (E) component of the model, which minimised any possible bias introduced by hypothetical measurement error, at least for the additive genetic (A) correlations (r_A) estimates.

In sum, our findings reveal that group-level results can overshadow substantial inter-individual differences within and between different neurobiological properties. Focusing on these previously underappreciated differences, we could highlight selective associations of individual variation in S-A axis cortical structure and function. These inter-individual differences and associations open a window into genetic sources of S-A axis structure and function, which we reveal to be selectively distinct. These results underscore the complex interplay between the S-A axis's structural and intrinsic functional properties, providing the readers with a set of tools that can be used to test their potential differential roles in shaping cognition.

Materials and Methods

Sample. We used data from the Human Connectome Project (HCP) S1200 release. The HCP includes data from 1206 individuals (656 women) that comprise 298 Monozygotic (MZ) twins, 188 Dizygotic (DZ) twins, and 720 singletons, with mean age ± *sd* = 28.8 ± 3.7 years (age range = 22-37 years). Informed consent for all individuals was obtained by HCP, and our data usage was approved by HCP and complied with all relevant ethical regulations for working with human participants (see (13, 25, 41)). The primary participant pool comes from individuals born in Missouri to families that include twins, sampled as healthy representatives of ethnic and socioeconomic diversity of US individuals, based on data from the Missouri Department of Health and Senior Services Bureau of Vital Records. We followed standard guidelines for inclusion criteria as described elsewhere (13). Our sample, in line with Valk et al., (13) comprised 992 (529 women) individuals. The first subsample of n = 482 (229 women) was created by excluding all individual twins. The second genetically informative subsample of n = 328 (212 women) was created by including only individual twins with genotyped zygosity matching self-reported zygosity (195 MZ and 133 DZ; 124 women and 88 women, respectively).

Functional imaging. Functional connectivity matrices were based on four 14 min 33 s of functional Magnetic Resonance Imaging (fMRI) data acquired over two sessions, spaced two days apart, through the HCP, which underwent HCP's minimal preprocessing. For each individual, four functional connectivity matrices were computed using the minimally preprocessed, spatially normalised resting-state fMRI (rsfMRI) scans, which were co-registered using MSMAll to template HCP 32k_LR surface space. 32k_LR surface space consists of 32,492 total nodes per hemisphere (59,412 excluding the medial wall). We computed four functional connectivity matrices per individual from the average time series extracted in each of the 400 Schaefer cortical parcels. The individual functional connectomes were generated by averaging preprocessed time series within nodes, Pearson correlating nodal time

series and converting them to Fisher-z scores. The average functional connectomes were obtained by averaging functional connectomes within individuals (i.e., between sessions) and between individuals.

Structural imaging. MRI protocols of the HCP have been previously described (25, 41). MRI data were acquired originally on the same day on the HCP's custom 3T Siemens Skyra equipped with a 32-channel head coil. T1w images with identical parameters were acquired using a 3D-MP-RAGE sequence over 7 min 40 s (0.7 mm isovoxels, matrix = 320 × 320, 256 sagittal slices; TR = 2400 ms, TE = 2.14 ms, TI = 1000 ms, flip angle = 8°; iPAT = 2). T2w images were acquired using a 3D T2-SPACE sequence with identical geometry over 8 min and 24 s (TR = 3200 ms, TE = 565 ms, variable flip angle; iPAT = 2). We followed the preprocessing steps outlined in Valk et al. (13).

Parcellation and functional networks. We used the Schaefer group-level hard-parcellation, originally obtained by a gradient-weighted Markov random field model integrating local gradient and global similarity approaches (26). To stratify results within established cortical functionally coupled networks, we used the seven Yeo-Krienen networks (42).

Microstructural profiles (T1w/T2w$_{mi}$). We used T1w/T2w imaging myelin-sensitive contrast from the HCP minimal processing pipeline, which uses the T2w to correct for inhomogeneities in the T1w image to estimate mean intensity T1w/T2w microstructural profiles (T1w/T2w$_{mi}$). T1w/T2w$_{mi}$ has been shown to map to model-based tract-tracing histological data in macaque, estimate intracortical myelin content, and thus approximate architectural complexity and cortical hierarchy (6).

Geodesic distance (GD). Individual Geodesic Distances (GD) were computed using the Micapipe toolbox (20). Briefly, we computed GD between each region and their top 10% of maximally functionally connected regions along each individual native cortical midsurface. We further averaged within regions to obtain a parcel-wise value and improve computation performance. Micapipe implements the Dijkstra algorithm (43) (further details can be found in (20)).

Functional gradient loadings (FC$_{G1}$). We sequentially averaged FCs, first within days, resulting in two FCs per individual, and then between days, resulting in one FC per individual. We then extracted the three first components from the two sequentially averaged and one averaged FCs, using the Python package BrainSpace (44). Extraction of the first eigenvector followed standard procedures, with the original individual FCs set at a connection density of 10% (i.e., the FCs were made sparse by setting a sparsity threshold of 90%). The first ten eigenvectors were then obtained by decomposing the FCs by diffusion map embedding, a robust non-linear manifold learning technique (1). To aid comparability across individuals, we aligned individual eigenvectors to the template eigenvector by Procrustes rotation (45). The template functional gradient was directly extracted from the overall mean FC matrix.

Group-level associations analysis. We computed Spearman rank-order correlations (ρ) between the structural (T1w/T2w$_{mi}$ and GD) and functional (FC$_{G1}$) S-A axis group-level properties. Group-level properties were obtained from the average of the individual structural S-A properties (i.e., average T1w/T2w$_{mi}$ and GD), and from the decomposition of the average FC (i.e., principal gradient obtained via diffusion map embedding of the average FC).

Measurement model of error in individual variability of the functional S-A axis. To partition stable inter-individual variability in functional gradient loading, we adapted previous measurement error models to rsfMRI to gradients (23, 24). The intuition behind such a modeling strategy is simple. Suppose parcel-wise values are measured without error and are stable over a reasonable period of time (e.g., one day). In that case, the correlations across individuals between the values obtained across two time points will equal 1. If the correlations deviate from 1 instead, regional values will be measured with some error, with bigger deviations corresponding to higher error or fluctuation over time. When errors, or changes over time, are present, we can use the measurement error model to estimate what stays constant across time, indexing the "true" regional values. Across the manuscript, for correctness, since "error" variance can include meaningful, yet unstable, fluctuation in rsfMRI, while "true" variance can also consist of systematic measurement error across sessions, we refer to the former term as intra-individual and the latter as inter-individual variability (28). First, we fit a measurement model to parcel-wise functional gradient loadings averaged within days. In line with Teeuw et al. (24), we did not constrain intra-individual variance components to be equal across days of scanning sessions. We performed model fitting in lavaan (44) after standardising observed variables (i.e., std.ov = T). We then used model estimates obtained for the variances of the latent and observed components. Using Spearman-Brown correction, we computed the averaged proportion of stable inter-individual variance in functional gradient loadings across days as the intra-class correlation (ICC) (46). For each parcel *i,* the ICC was calculated as follows:

$$\mathrm{ICC}(2,k)_{(\mathrm{i})} = \frac{\mathrm{k} * \mathrm{ICC}(2,1)_{(\mathrm{i})}}{1 + (k-1) * \mathrm{ICC}(2,1)_{(\mathrm{i})}}$$

Where k is a constant equal to the number of measures (i.e., k = 2) and the $\mathrm{ICC}(2,1)_{(i)}$ is calculated as follows:

$$\mathrm{ICC}(2,1)_{(\mathrm{i})} = \frac{\sigma^2_{\mathrm{inter(i)}}}{\sigma^2_{\mathrm{inter(i)}} + (\frac{\sigma^2_{1-\mathrm{intra(i)}} + \sigma^2_{2-\mathrm{intra(i)}}}{2})}$$

$\mathrm{ICC}(2,k)_{(i)}$ estimates the proportion of inter-individual variance over the total variance, $\sigma_{inter}{}^2{}_{(i)}$, in the functional loadings as if they were obtained from the average of the two scanning sessions. The proportion of intra-individual variance for a parcel i, $\sigma_{intra}{}^2{}_{(i)}$, is obtained simply by subtracting the $\mathrm{ICC}(2,k)_{(i)}$ from 1.

The expected bias for any parcel i was calculated following Tiego et al. (22):

$$\mathrm{bias}_{(\mathrm{i})} = \sqrt{R_{\mathrm{p,p}} * R_{\mathrm{FCG1,FCG1(i)}}}$$

Where $R_{p,p}$, the reliability for the structural S-A axis property p (e.g., T1w/T2w$_{mi}$), was set to be equal to 1 across all parcels, and $R_{FCG1,FCG1(i)}$, the reliability of parcel-wise value for the functional gradient loading, was calculated as $\mathrm{ICC}(2,k)_{(i)}$.

Structural Measurement Error Equation Modeling. We used Structural Equation Modeling (SEM) to estimate correlations between structural (i.e., $T1w/T2w_{mi(i)}$,$GD_{(i)}$) and functional (i.e, $FC_{G1(i)}$) S-A modalities. Each multivariate model simultaneously accounted for intra-individual variances by including the measurement error model. All models were fitted in lavaan (47) after standardising all observed variables (i.e., std.ov = T). Prior to model fitting, sex and age were regressed from parcel-wise S-A axis values using the function umx::umx_residualize() (48). Structural equation models were fit to residual scores. We assumed missing data to be missed at random and followed parameters' estimation via full-information Maximum Likelihood (i.e., missing = "ML").

Twin-informed Multivariate Structural Equation Modeling. We used multigroup SEM to partition parcel-wise variability in structural ($\sigma^2 T1w/T2w_{mi(i)}$, $\sigma^2 GD_{(i)}$) and functional ($\sigma_{inter}{}^2{}_{(i)}$) S-A modalities into either additive genetic ($\sigma^2{}_A$) and unsystematic environmental ($\sigma^2{}_E$) sources of variance. Structural equation models were fit to $T1w/T2w_{mii}$, GD_i, and FC_{G1i1} (day 1) and FC_{G1i2} (day 2) data, grouped by zygosity (i.e., two groups). The model specification was informed by the multivariate twin design (49). Briefly, monozygotic (MZ) twins are ~100 % genetically identical, coming from the same fertilised egg. In contrast, dizygotic (DZ) twins are, on average, only 50% additively genetically similar regarding allelic variants coming from two different fertilised eggs. Thus, the correlation between the additive genetic component (A) is set to be equal to 1 for MZ while .5 for DZ. In contrast, each twin's unique environment (E) component will be unique; therefore, their correlation will be equal to 0. In total, we fit one multivariate AE model per parcel. Following the measurement error procedure outlined above and (24), a common pathway measurement error model was included in the specification of the multigroup SEM. As such, each multivariate model simultaneously accounted for intra-individual variance. We employed the direct symmetric approach by estimating variance components directly while setting path coefficients to 1 (with the exception of the measurement model, for which we fixed the variance to be equal to 1, and estimated the path coefficients, instead). We chose this approach as it has been shown to reduce type I errors and produce asymptotically unbiased χ^2 (50).

All models were fitted in lavaan (47), with standardisation of observed variables before model fitting (i.e., std.ov = T). Similarly to what was reported above, to control for the effect of age and sex on S-A axis properties, we residualised parcel-wise variables prior to modeling using the function umx::umx_residualize() (48). Residuals were used as observed variables in later twin modeling. We estimated parameters via full-information Maximum Likelihood (i.e., missing = "ML") and evaluated the goodness of fit for each parcel by comparative fit index (CFI) and root mean square error of approximation (RMSEA) scores. Following standard cut-offs (24), we retained only models with a "satisfactory" CFI>.90 and an RMSEA<.08. Narrow-sense twin heritability ($h^2{}_{twin}$) estimates for each parcel *i* were defined as the ratio of the additive genetic variance over the sum of the additive genetic and environmental variances:

$$h^2{}_{twin\text{-}p(i)} = \frac{\sigma^2_{Ap(i)}}{\sigma^2_{Ap(i)} + \sigma^2_{Ep(i)}}$$

Where $\sigma^2_{Ap(i)}$ is the additive genetic variance for the S-A axis parcel-wise value for the given property *p* (e.g., GD). For functional gradient loadings, the heritability was calculated as

$$h^2_{\text{twin-inter(i)}} = \sigma^2_{\text{Ainter(i)}}$$

After imposing the equality constrain on the common factor $FC_{G1inter(i)}$

$$\sigma^2_{\text{Ainter(i)}} + \sigma^2_{\text{Einter(i)}} = 1$$

Genetic correlations (r_A) were calculated as:

$$r_A = \frac{\sigma_{\text{Ap1i,Ap2i}}}{\sqrt{\sigma^2_{\text{Ap1i}} * \sigma^2_{\text{Ap2i}}}}$$

Where $\sigma_{Ap,Ap2}$ is the additive genetic covariance between two S-A axis property *p1* and *p2* (e.g., GD and $T1w/T2w_{mi}$). Environmental correlations were calculated similarly to r_A but using environmental variance and covariances estimates.

Generalisation beyond regional associations. For each individual, we obtain two metrics for structural and functional S-A axis properties (i.e., a total of six measures per individual) :

Overall within-individual Median Absolute Deviation: we quantified the spread of the regional values across the cortex by computing within-individual Median Absolute Deviation (MAD) of microstructure, geodesic distances, and functional gradient loadings. MAD is a robust univariate measure of statistical dispersion and is simply calculated as follows:

$$MAD_{pj} = med(|p_{pji} - med(p_{pj})|)$$

Where p_{ij} is the parcel-wise value for a property *p*, an individual *j*, and a parcel *I* and *med* is the median.

ρ similarity index: we obtained the similarity index by estimating the Spearman rank (*ρ*) correlations between each individual microstructure, cortico-cortical network proximity, and functional gradient loadings with the respective S-A group-level modality vectors. For example, the *ρ* similarity index for the cortico-cortical network proximity for an individual *j* was obtained by correlating their GD with the group-level GD. Similarly, for the same individual *j*, the similarity index for their functional gradient loading was obtained by correlating their FC_{G1} on day 1 and on day 2 of scanning with the group-level FC_{G1}.

Similar to what is outlined above for regional analysis, we fit two multivariate AE models, one per metric. Before model fitting, *ρ* similarity indices were first Fisher-z transformed. To recapitulate regional analysis as closely as possible within the multivariate model, we also included the measurement error model to overall within-individual MAD and *ρ* similarity index functional gradient loadings obtained on days 1 and 2 of scanning sessions. Note that standardised coefficients are obtained using the lavaan::standardizedSolution() function. As a final sensitivity analysis, to discount individuals' whole brain volume as a possible confounding effect of the relationship between SA axis structure-function associations, we additionally included total Intra-Cranial volume (ICV). Precisely, we followed a two-

step procedure to discount ICV as a possible common cause. First, we regressed out ICV from overall within-individual MAD and Fisher-z transformed ρ similarity indices for all S-A axis properties. We then re-fit the exact multivariate twin models to the residuals.

Data availability

We obtained human data from the open-access Human Connectome Project (HCP) S1200 young adult sample. HCP Young Adult data are available at https://www.humanconnectome.org/study/hcp-young-adult. Supporting Files 1-5 with summary statistics can be found at https://github.com/giacomobignardi/h2_SA_axis/tree/main/SI.

Code availability

All code is available and can be found at https://github.com/giacomobignardi/h2_SA_axis . SEM and twin-based analysis have been done using the statistical package latent variable analysis (lavaan) https://lavaan.ugent.be/. The function to apply the measurement error model (meermo) can be found here https://github.com/giacomobignardi/h2_SA_axis/tree/main/R/functions/meermo. lavaan syntax for latent variable analysis of twin data (lavaantwda) can be found following the repository https://github.com/giacomobignardi/h2_SA_axis/tree/main/R/functions/lavaantwda. An introduction to twin modeling using lavaan can be found at https://rpubs.com/MichelNivard/798608. Code and tutorial for functional gradient decomposition of functional connectomes are available at https://brainspace.readthedocs.io/en/latest/pages/install.html. The code and tutorial to generate geodesic distances can be found at https://micapipe.readthedocs.io/en/latest/.

Acknowledgements

We want to thank the Human Connectome Project, Washington University, the University of Minnesota, and Oxford University Consortium (Principal Investigators: David Van Essen and Kamil Ugurbil; 1U54MH091657) originally funded by the 16 N.I.H. Institutes and Centers that support the N.I.H. Blueprint for Neuroscience Research; and by the McDonnell Center for Systems Neuroscience at Washington University. We would also like to thank Jitse Amelink, Meike D. Hettwer, and MacKenzie D. Trupp for their comments on an earlier version of the draft. Furthermore, we would like to thank the Max Planck School of Cognition. This study was supported by the German Federal Ministry of Education and Research (BMBF) and the Max Planck Society.

568 **References**

569 1. D. S. Margulies, *et al.*, Situating the default-mode network along a principal gradient of
570 macroscale cortical organization. *Proc. Natl. Acad. Sci.* **113**, 12574–12579 (2016).

571 2. M. M. Mesulam, From sensation to cognition. *Brain* **121**, 1013–1052 (1998).

572 3. V. J. Sydnor, *et al.*, Neurodevelopment of the association cortices: Patterns, mechanisms, and
573 implications for psychopathology. *Neuron* **109**, 2820–2846 (2021).

574 4. V. J. Sydnor, *et al.*, Intrinsic activity development unfolds along a sensorimotor–association
575 cortical axis in youth. *Nat. Neurosci.* **26**, 638–649 (2023).

576 5. C. F. von Economo, G. N. Koskinas, Die cytoarchitektonik der hirnrinde des erwachsenen
577 menschen. *J Springer* (1925).

578 6. J. B. Burt, *et al.*, Hierarchy of transcriptomic specialization across human cortex captured by
579 structural neuroimaging topography. *Nat. Neurosci.* **21**, 1251–1259 (2018).

580 7. K. Brodmann, ergleichende Lokalisationslehre der Grosshirnrinde in ihren Prinzipien dargestellt
581 auf Grund des Zellenbaues. *Barth* (1909).

582 8. M. Ercsey-Ravasz, *et al.*, A predictive network model of cerebral cortical connectivity based on a
583 distance rule. *Neuron* **80**, 184–197 (2013).

584 9. R. L. Buckner, F. M. Krienen, The evolution of distributed association networks in the human
585 brain. *Trends Cogn. Sci.* **17**, 648–665 (2013).

586 10. M. Á. García-Cabezas, J. L. Hacker, B. Zikopoulos, Homology of neocortical areas in rats and
587 primates based on cortical type analysis: an update of the Hypothesis on the Dual Origin of the
588 Neocortex. *Brain Struct. Funct.* **228**, 1069–1093 (2023).

589 11. A. Saberi, *et al.*, The regional variation of laminar thickness in the human isocortex is related to
590 cortical hierarchy and interregional connectivity. *PLoS Biol.* **21**, e3002365 (2023).

591 12. N. T. Markov, *et al.*, Cortical high-density counterstream architectures. *Science* **342**, 1238406
592 (2013).

593 13. S. L. Valk, *et al.*, Genetic and phylogenetic uncoupling of structure and function in human
594 transmodal cortex. *Nat. Commun.* **13**, 2341 (2022).

595 14. M. Demirtaş, *et al.*, Hierarchical Heterogeneity across Human Cortex Shapes Large-Scale Neural
596 Dynamics. *Neuron* **101**, 1181-1194.e13 (2019).

597 15. C. Paquola, K. Amunts, A. Evans, J. Smallwood, B. Bernhardt, Closing the mechanistic gap: the
598 value of microarchitecture in understanding cognitive networks. *Trends Cogn. Sci.* **26**, 873–886
599 (2022).

600 16. R. Leech, *et al.*, Variation in spatial dependencies across the cortical mantle discriminates the
601 functional behaviour of primary and association cortex. *Nat. Commun.* **14**, 5656 (2023).

602 17. L. E. Suárez, R. D. Markello, R. F. Betzel, B. Misic, Linking Structure and Function in Macroscale
603 Brain Networks. *Trends Cogn. Sci.* **24**, 302–315 (2020).

604 18. J. M. Huntenburg, P.-L. Bazin, D. S. Margulies, Large-Scale Gradients in Human Cortical
605 Organization. *Trends Cogn. Sci.* **22**, 21–31 (2018).

606 19. E. A. Willoughby, T. J. C. Polderman, B. B. Boutwell, Behavioural genetics methods. *Nat. Rev.*
607 *Methods Primer* **3**, 1–16 (2023).

20. R. R. Cruces, *et al.*, Micapipe: A pipeline for multimodal neuroimaging and connectome analysis. *NeuroImage* **263**, 119612 (2022).

21. K. Helwegen, I. Libedinsky, M. P. van den Heuvel, Statistical power in network neuroscience. *Trends Cogn. Sci.* **27**, 282–301 (2023).

22. J. Tiego, *et al.*, Precision behavioral phenotyping as a strategy for uncovering the biological correlates of psychopathology. *Nat. Ment. Health* **1**, 304–315 (2023).

23. A. M. Brandmaier, *et al.*, Assessing reliability in neuroimaging research through intra-class effect decomposition (ICED). *eLife* **7**, e35718 (2018).

24. J. Teeuw, H. E. Hulshoff Pol, D. I. Boomsma, R. M. Brouwer, Reliability modelling of resting-state functional connectivity. *NeuroImage* **231**, 117842 (2021).

25. D. C. Van Essen, *et al.*, The Human Connectome Project: A data acquisition perspective. *NeuroImage* **62**, 2222–2231 (2012).

26. A. Schaefer, *et al.*, Local-Global Parcellation of the Human Cerebral Cortex from Intrinsic Functional Connectivity MRI. *Cereb. Cortex* **28**, 3095–3114 (2018).

27. S.-J. Hong, *et al.*, Atypical functional connectome hierarchy in autism. *Nat. Commun.* **10**, 1022 (2019).

28. X.-N. Zuo, T. Xu, M. P. Milham, Harnessing reliability for neuroscience research. *Nat. Hum. Behav.* **3**, 768–771 (2019).

29. F. A. Hagenbeek, *et al.*, Maximizing the value of twin studies in health and behaviour. *Nat. Hum. Behav.* **7**, 849–860 (2023).

30. D. S. Falconer, T. F. C. Mackay, *Introduction to Quantitative Genetics*, 4 edition (Pearson, 1996).

31. T. O. Laumann, A. Z. Snyder, Brain activity is not only for thinking. *Curr. Opin. Behav. Sci.* **40**, 130–136 (2021).

32. J. M. Shine, M. J. Aburn, M. Breakspear, R. A. Poldrack, The modulation of neural gain facilitates a transition between functional segregation and integration in the brain. *eLife* **7**, e31130 (2018).

33. A. I. Luppi, *et al.*, In vivo mapping of pharmacologically induced functional reorganization onto the human brain's neurotransmitter landscape. *Sci. Adv.* **9**, eadf8332 (2023).

34. D. Dong, *et al.*, Compressed sensorimotor-to-transmodal hierarchical organization in schizophrenia. *Psychol. Med.* **53**, 771–784 (2023).

35. M. Xia, *et al.*, Connectome gradient dysfunction in major depression and its association with gene expression profiles and treatment outcomes. *Mol. Psychiatry* **27**, 1384–1393 (2022).

36. S. Marek, *et al.*, Reproducible brain-wide association studies require thousands of individuals. *Nature* **603**, 654–660 (2022).

37. T. Xu, *et al.*, ReX: an integrative tool for quantifying and optimizing measurement reliability for the study of individual differences. *Nat. Methods* **20**, 1025–1028 (2023).

38. H. van Kippersluis, *et al.*, Overcoming attenuation bias in regressions using polygenic indices. *Nat. Commun.* **14**, 4473 (2023).

39. J. N. Pritikin, M. C. Neale, E. C. Prom-Wormley, S. L. Clark, B. Verhulst, GW-SEM 2.0: Efficient, Flexible, and Accessible Multivariate GWAS. *Behav. Genet.* **51**, 343–357 (2021).

40. A. D. Grotzinger, *et al.*, Genomic structural equation modelling provides insights into the multivariate genetic architecture of complex traits. *Nat. Hum. Behav.* **3**, 513–525 (2019).

41. M. F. Glasser, *et al.*, The minimal preprocessing pipelines for the Human Connectome Project. *NeuroImage* **80**, 105–124 (2013).

42. B. T. T. Yeo, *et al.*, The organization of the human cerebral cortex estimated by intrinsic functional connectivity. *J. Neurophysiol.* **106**, 1125–65 (2011).

43. E. W. Dijkstra, A note on two problems in connexion with graphs. *Numer. Math.* **1**, 269–271 (1959).

44. R. Vos de Wael, *et al.*, BrainSpace: a toolbox for the analysis of macroscale gradients in neuroimaging and connectomics datasets. *Commun. Biol.* **3**, 1–10 (2020).

45. R. A. I. Bethlehem, *et al.*, Dispersion of functional gradients across the adult lifespan. *NeuroImage* **222**, 117299 (2020).

46. T. K. Koo, M. Y. Li, A Guideline of Selecting and Reporting Intraclass Correlation Coefficients for Reliability Research. *J. Chiropr. Med.* **15**, 155–163 (2016).

47. Y. Rosseel, lavaan: An R Package for Structural Equation Modeling. *J. Stat. Softw.* **48**, 1–36 (2012).

48. T. C. Bates, H. Maes, M. C. Neale, umx: Twin and Path-Based Structural Equation Modeling in R. *Twin Res. Hum. Genet. Off. J. Int. Soc. Twin Stud.* **22**, 27–41 (2019).

49. D. Boomsma, A. Busjahn, L. Peltonen, Classical twin studies and beyond. *Nat. Rev. Genet.* **3**, 872–882 (2002).

50. B. Verhulst, E. Prom-Wormley, M. Keller, S. Medland, M. C. Neale, Type I Error Rates and Parameter Bias in Multivariate Behavioral Genetic Models. *Behav. Genet.* **49**, 99–111 (2019).

51. A. M. Mowinckel, D. Vidal-Piñeiro, Visualization of Brain Statistics With R Packages ggseg and ggseg3d. *Adv. Methods Pract. Psychol. Sci.* **3**, 466–483 (2020).

Figures

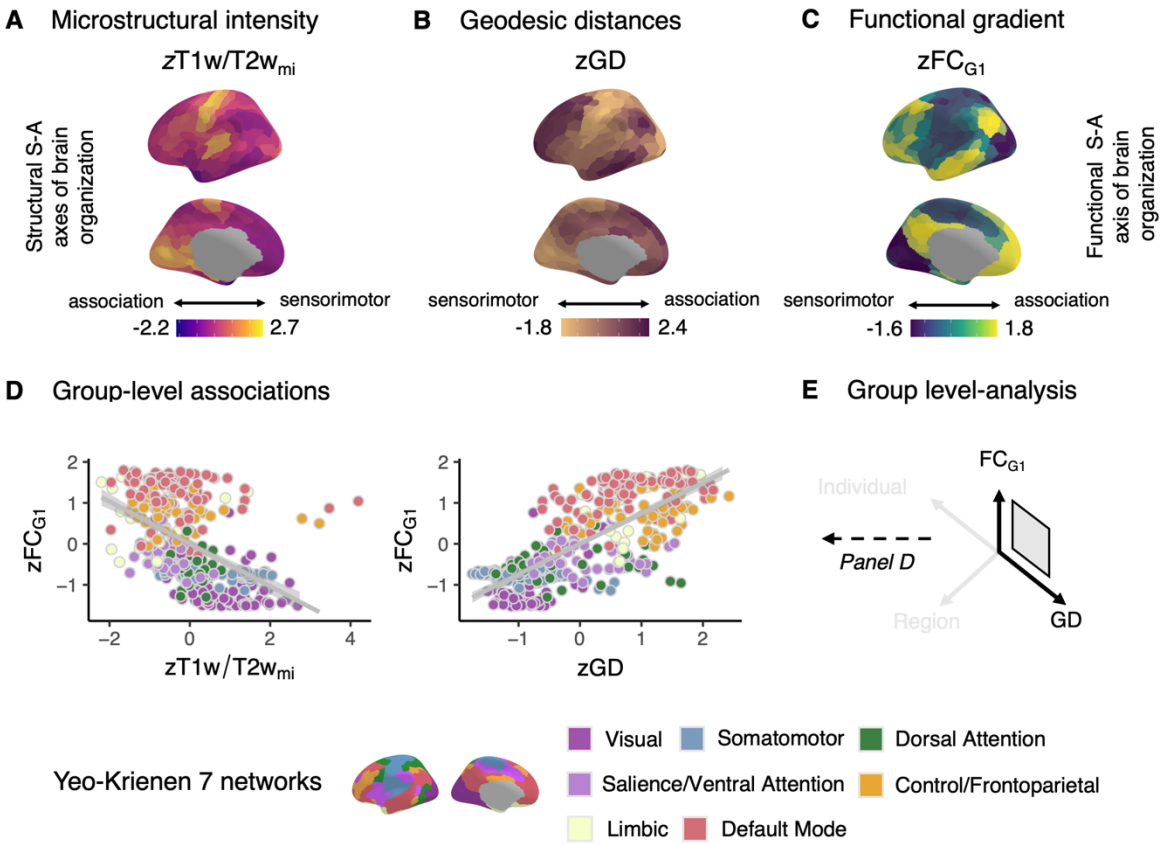

Figure 1. Structural and functional S-A axes strongly correlate at the group-level. Structural (**A-B**) and functional (**C**) indices of Sensorimotor-Association (S-A) axes plotted on inflated cortical surfaces (51). Values represent averages of individual T1w/T2w mean intensity profiles (A; T1w/T2w$_{mi}$), averages of individual Geodesic Distances (B; GD), and functional gradients loadings (C; FC$_{G1}$) extracted from the average of individual functional connectomes across 400 cortical regions. (**D**) Structural indices are strongly associated with functional indices of the S-A axis; Spearman ρ=-.61 and ρ=.75 between T1w/T2w$_{mi}$ and FC$_{G1}$, and GD and FC$_{G1}$, respectively; all p<.05). Each dot represents a regional value; the colour represents Yeo-Krienen 7 network membership. (**E**) Conceptual representation of group-level analysis. Note that individual and regional information is lost in favour of group-level results.

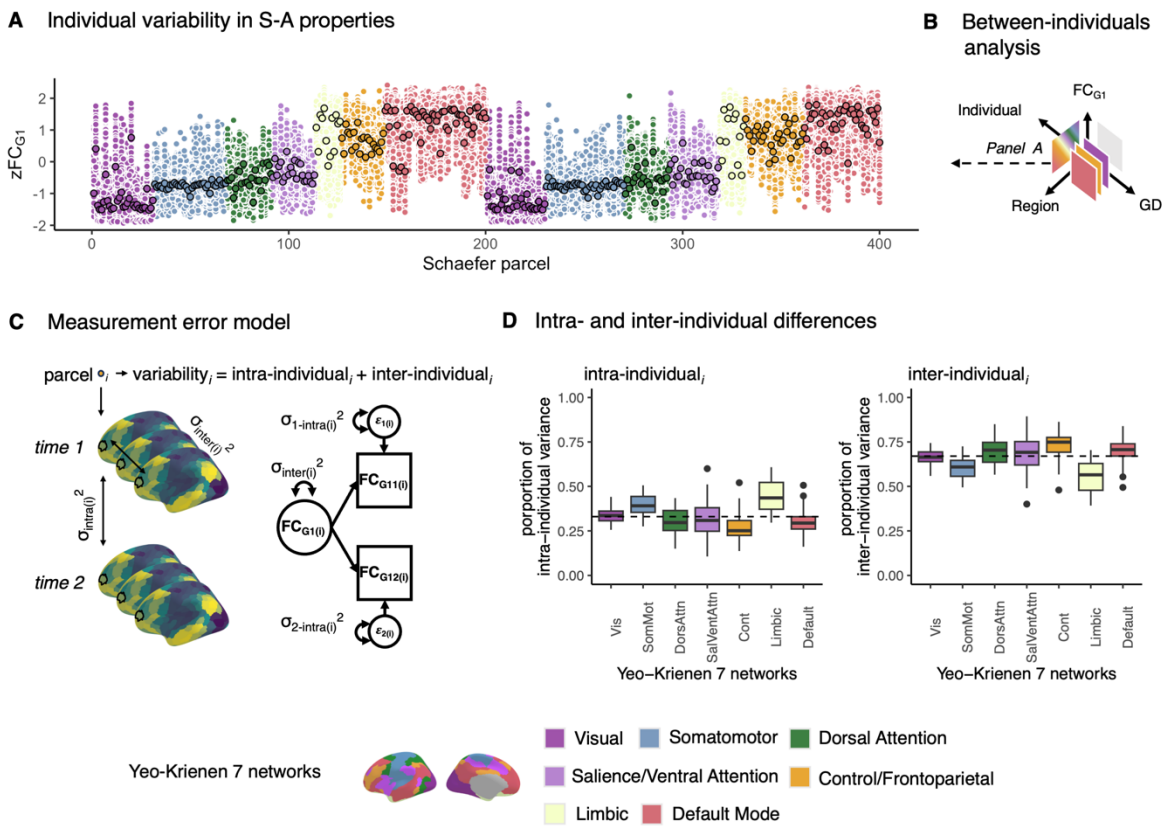

Figure 2. Pervasive inter-individual differences in the S-A axis of functional connectivity. (**A**) group-level estimates (black contour) overshadow pervasive individual differences in S-A axis properties. (**B**) The shift between levels of analyses: from group-level (grey square) to between-individuals (coloured squares); The gradient square conceptually captures panel A. (**C**) Conceptual and formal measurement error model to partition, for any parcel *i*, variance in the functional gradient loadings into intra- ($\sigma_{d\text{-}intra(i)}^2$, for regional values measured at day 1 or 2 of the testing session, i.e., squares) and inter- ($\sigma_{inter(i)}^2$, for the latent component, i.e., circle) individual variance. Parameter estimates for any parcel *i* can be found in Supporting File 1. (**D**) The proportion of intra- and inter-individual variance in the functional network across Yeo-Krienen functional networks: the horizontal line displays the median; lower and upper hinges correspond to the first and third quartile; the whisker extends from the hinge to the largest/lower value no further than 1.5 * interquartile range from the hinge. Note that across all parcels, observed variance includes substantial inter-individual variation. *Notes on measurement model: Squares represent the measured phenotypes; The circle is the latent component; the double-headed arrows within the circle represent the variance associated with the latent components; one-headed arrows are the paths (here all set to 1).*

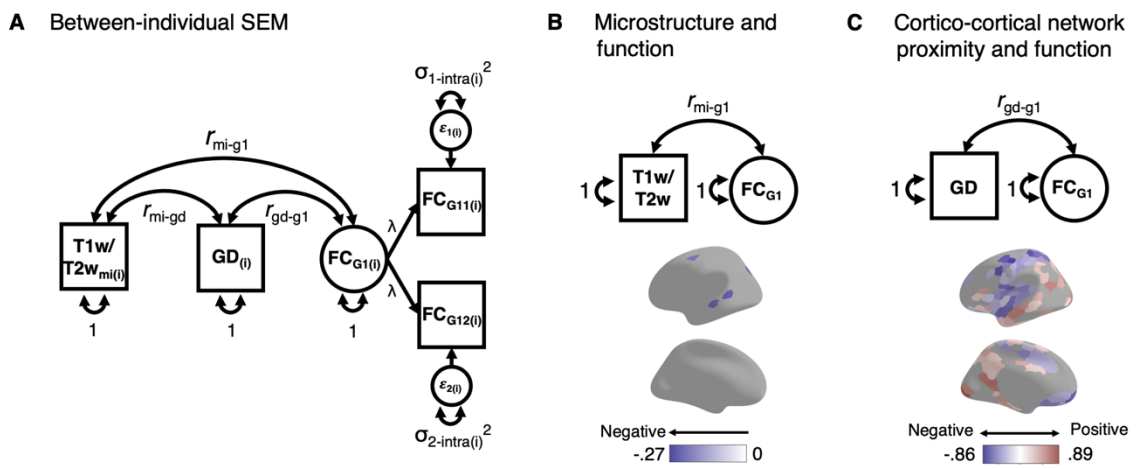

Figure 3. Structural and functional S-A axes selectively correlate between individuals. (**A**) Simplified structural measurement error model to estimate the correlation between S-A axis properties considering the distinction between intra- and inter-individual differences in functional gradient loading variability. Observed parcel-wise values and latent components are standardised before model fitting. (**B-C**) Summary for the standardised estimates on the inflated cortical surface (51) from the structural measurement error model indicates little and weak overlaps between microstructural intensity ($T1w/T2w_{mi}$) and functional gradient loadings (FC_{G1}) inter-individual differences but large and highly significant (p<.05 corrected for Bonferroni comparisons) overlaps between functional gradient loadings and geodesic distances (GD). All parameter estimates for any parcel *i*, including the covariances between $T1w/T2w_{mi}$ and GD that were not the focus of the current study, can be found in Supporting File 2. *Notes on structural equation models: double-headed arrows between circles represent covariances; here, path coefficients for the measurement error model are estimated (λ). Other abbreviations and symbols are as in Figure 2.*

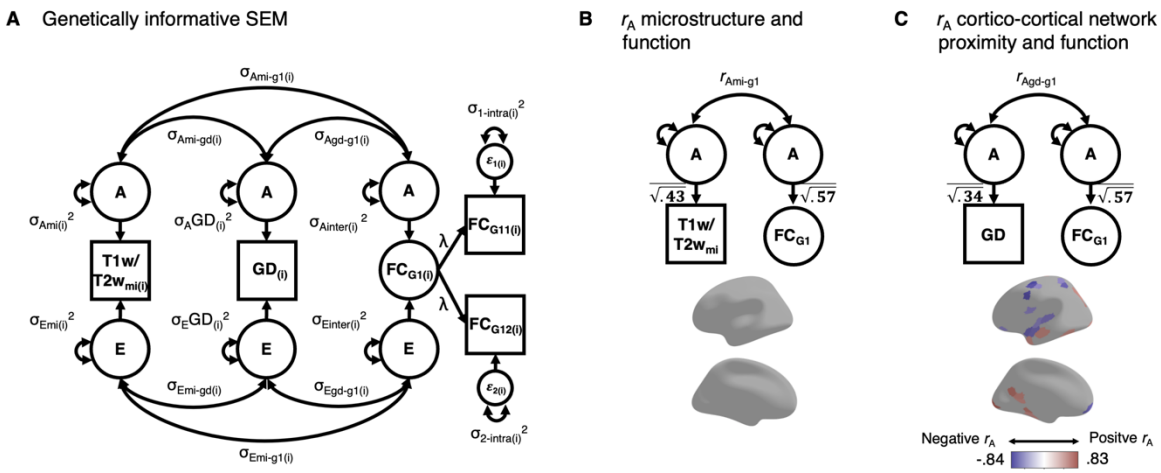

Figure 4. Genetic sources of the S-A axis' structural and functional properties are selectively distinct. (**A**) Simplified graphical representation of the multivariate twin-informed SEM. All parameter estimates for any parcel *i* can be found in Supporting File 3**.** (**B-C**) simplified summary for the significant additive genetic correlations (r_A) across S-A axis properties on the inflated cortical surface (46) indicates only significant genetic correlations between cortico-cortical network proximity, as measured by geodesic distances (GD) and functional gradients loadings (FC_{G1}). Note that since we report here (average) standardised path coefficient estimates, the double-headed arrow between the two additive genetic components can now be interpreted as r_A. r_A estimates can be found in Supporting Files 4-5 (B-C, respectively). *Notes on structural equation models: additional circles represent latent additive genetic and environmental components; Double-headed arrows between circles represent genetic and environmental covariances. Where not noted, path coefficients are set to 1. Other abbreviations and symbols are as in Figure 2.*

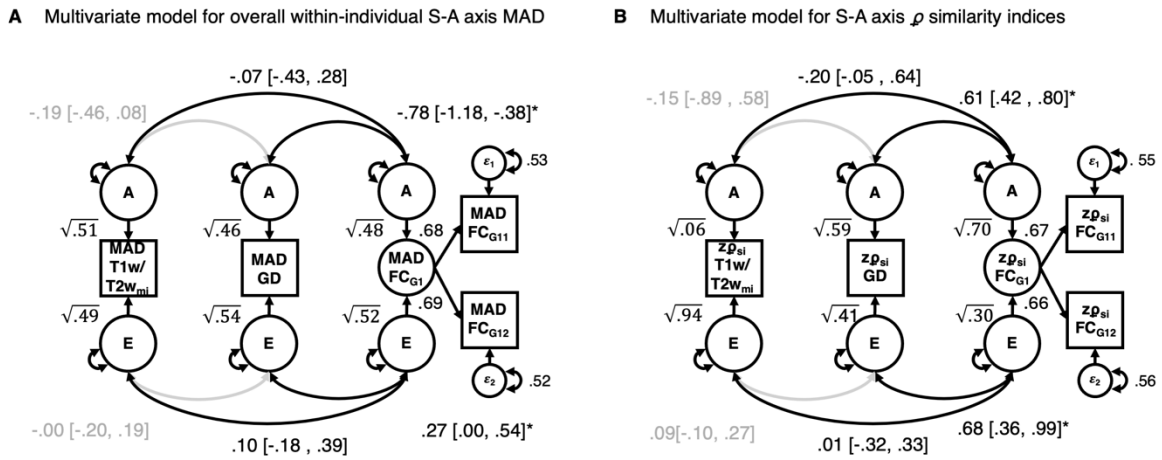

Figure 5. Findings extend beyond regional S-A axis associations. (A) Simplified graphical representation of the multivariate twin-informed SEM for overall within-individual Median Absolute Deviations (MAD). Note the strong but negative significant associations between the latent additive genetic components underlying geodesic distances (GD; centre) and functional gradient loadings ($FC_{G1;}$ right). **(B)** Simplified graphical representation of the multivariate twin-informed SEM for ρ similarity indices (Fisher-z transformed). As for the model reported in panel A, the only significant associations are found between GD and FC_{G1}. * $p < .05$. *Notes on structural equation models: abbreviations and symbols are as in Fig. 4. Here, double-headed arrows between latent variables indicate correlations (since we report standardised solutions).*